# Wet and Dry Cold Surges over the Maritime Continent

**I. Tan[1], M. J. Reeder[1,2], M. S. Singh[1,2], C. E. Birch[3], and S. C. Peatman[3]**

[1] School of Earth, Atmosphere and Environment, Monash University, Clayton, Victoria, Australia

[2]Australian Research Council Centre for Climate Extremes, Australia

[3] Institute of Climate and Atmospheric Science, School of Earth and Environment, University of Leeds, Leeds, United Kingdom

Corresponding author: Isaac Tan (isaac.tan@monash.edu)

**Key Points:**

- The synoptic structure and development of dry, moderate, and wet cold surge composites over the Maritime Continent are investigated.
- Wet cold surges are characterised by a moister free troposphere that allows convection to penetrate the lower troposphere.
- Australian summer monsoon bursts are more likely to follow dry cold surges, and are primarily influenced by the Madden Julian Oscillation.

## Abstract

Cold surges are synoptic weather systems that occur over the Maritime Continent during the boreal winter. They are characterised by the strengthening of prevailing low-level northerly to north-easterly winds, temperature falls of a few degrees over several days, and in some cases, extreme prolonged rainfall and flooding. We investigate the synoptic structure and development of cold surges through composites of dry, moderate and wet surges. Each surge category is defined by the distribution of precipitation averaged within a specified domain over the equatorial South China Sea.

Over the Maritime Continent, most of the dry (wet) surges occur during the suppressed (active) phases of the Madden-Julian Oscillation (MJO). Dry surges are characterised by cross-equatorial flow and positive mean sea-level pressure anomalies which reach the Southern Hemisphere, and enhanced descent or weaker ascent. Wet surges coincide with a cyclonic circulation over Borneo, a lack of cross-equatorial flow, and enhanced moisture and ascent. We find that diurnal precipitation patterns are consistent with convective onset being controlled by the mid-tropospheric buoyancy of an idealised entraining plume. This buoyancy diagnostic suggests that wet surges are characterised by a moister free troposphere because this reduces the effect of entrainment and allows convection to penetrate the lower troposphere.

Finally, deep (shallow) and relatively strong (weak) westerlies are found over southern Java and northern Australia during the dry (wet) surges. Consequently, Australian summer monsoon bursts are more likely to occur following dry cold surges. The westerlies are also explained as part of the larger-scale MJO circulations.


## Plain Language Summary

Cold surges are large-scale monsoon weather systems that bring enhanced north-easterly winds, colder temperatures, and often extreme rainfall and flooding over the Maritime Continent region between November and March each year. We investigate the structure and development of dry, moderate, and wet cold surges. The three categories are defined based on rainfall averages over a domain located near the equator, and are largely influenced by the Madden-Julian Oscillation (MJO), which is the major fluctuation in tropical weather on weekly to monthly timescales. Of the three categories, we find that dry surges are characterized by the highest pressure, and north-easterly winds from the surge cross the equator into the Southern Hemisphere, which then turn to become westerly. As a result, relatively strong westerly winds are found over southern Java and northern Australia during dry surges, leading to bursts in the Australian summer monsoon. In contrast, wet surges coincide with a cyclonic circulation over Borneo and increased moisture and convection, and there are a lack of westerly winds over southern Java and northern Australia.

## 1 Introduction

Cold surges are synoptic weather systems that occur over the Maritime Continent during the boreal winter (November-March; NDJFM), and are characterised by the strengthening of prevailing low-level northerly to north-easterly winds, temperature falls of a few degrees over several days, and in some cases, extreme prolonged rainfall and flooding (e.g. Ramage 1971; Chang et al., 1979; Ding, 1994; Chang et al., 2004; Chang et al., 2005, Johnson and Chang 2007; Wu et al 2007; Tangang et al., 2008; Fong and Ng, 2012; Pullen et al., 2015; Lim et al., 2017; Xavier et al., 2020; MSS, 2022). They often produce bursts of convection around the equator, affecting the coastal regions of South East Asia such as Vietnam, the Malaysian Peninsula, and Singapore. These regions are located within the western half of the Maritime Continent, which is

the largest archipelago on Earth and a region of intense convection (e.g., Ramage, 1968; Neale and Slingo, 2003; Argüeso et al., 2020).

Examples of extreme rainfall from cold surges are documented in Fong and Ng (2012), including one on 9-10 December 1969 where torrential rainfall over the east coast of the Malaysian Peninsula was observed, and a daily rainfall total of 483.1 mm was recorded at Singapore's climate station. During another cold surge on 2 December 1978, a record high daily rainfall total of 512.4 mm was observed, which is about 25% of Singapore's annual average rainfall (Fong and Ng, 2012). The extreme rainfall from this surge resulted in seven deaths and the evacuation of hundreds due to widespread flooding over the island. More recently, two strong cold surges that affected Singapore and the surrounding region between 1–2 January and 8–13 January 2021 each had peak daily rainfall amounts exceeding 200 mm at Singapore's climate station. These consecutive cold surges were the primary contributors of the second wettest January in 152 years of record (MSS, 2022a).

Cold surges are driven by the strengthening of a large anticyclone over Siberia that dominates the low-level circulation over Asia, often referred to as the "Siberian high" (e.g., Lim and Chang, 1981; Lau and Li, 1984; Yihui, 1994; Fong and Ng, 2012). Southward intrusions of the Siberian high often result in sudden surges of strong northerly to north-easterly winds that propagate towards China and the South China Sea. As cold and dry winds strengthen equatorward with the passage of the surge, their air temperature and humidity increase, and is associated with warmer equatorial sea surface temperatures (Chang et al., 1979, 1983). In response to the strengthening low-level winds, a cyclonic circulation often forms off the northwest coast of Borneo, which is known as the Borneo vortex and is associated with enhanced deep convection (e.g., Chang et al., 1979; Johnson and Houze, 1987; Chang et al., 2003; Chang et al., 2005).

From November to January, heavy rainfall from cold surges often affects Vietnam, the Malaysian Peninsula, and Singapore (Fong and Ng, 2012; MSS, 2022a). Between February and March, cold surges cross the equator about 75% of the time, resulting in drier conditions over the entire Malaysian Peninsula, eastern Vietnam, and Sumatra, but enhanced rainfall over the Java Sea and northwest of Australia (Xavier et al., 2020). It is also thought that cross-equatorial surges sometimes trigger the onset of the Australian summer monsoon (e.g., Davidson et al., 1983; Love, 1985; Suppiah and Wu, 1998). The relative importance of cross-equatorial surges to the onset of, and bursts in, the Australian summer monsoon compared to other influences such as midlatitude fronts and the Madden-Julian Oscillation (MJO; e.g., Berry and Reeder, 2016; Narsey et al., 2017; Narsey et al., 2018) have not yet been investigated.

Yang et al. (2019) examined the conditions for both wet and dry cold surges over Singapore during NDJFM 1979-80 to 2017-18. They found that wet cold surges are characterised by a strengthening of the moisture flux in the South China Sea, positive moisture flux convergence anomalies between 0°N and 10°N two days before surge onset, and heavy rainfall over Singapore on the day of onset. In contrast, dry surges exhibit negative moisture flux anomalies from 0°N–15°N and positive anomalies from 0°S–12°S up to 5 days prior to the surge. Consistent with cross-equatorial surges, these dry surges mostly occur later in the boreal winter season between January and February.

Cold surges lasting 6 or more days that reach the low latitudes and exhibit distinct precipitation signatures over the Maritime Continent region were classified into 4 types by Abdillah et al. (2021). Of the four surge types, two are relevant to the equatorial Maritime Continent region, namely the ‘South China Sea type’ and ‘Both type’. The former mostly occurs in the early winter months and is often associated with low-pressure vortices near Borneo leading

to heavy rainfall or flooding over South East Asia, whereas the latter is a combination of surges that affect both the South China Sea and the Philippines Sea, and is characterised by the strong southward propagation of both northerly wind and high-pressure anomalies that cross the equator. These surges are also characterised by strong positive precipitation anomalies over the South China Sea, western Maritime Continent, and Java.

According to Chang et al. (2005), the MJO modulates the frequency of cold surges and contributes to variability in deep convection. The impact of deep convection is also affected by the Borneo vortex, and its interaction with cold surges and the MJO. Chang et al. (2005) find that cold surges enhance the contrast of enhanced (suppressed) deep convection over the South China Sea when the Borneo vortex is present (absent). Cold surges strengthen the vortex and shift the vortex centre from being located over the South China Sea to the western coast of Borneo. The strong cyclonic horizontal shear over Borneo associated with enhanced equatorial westerly winds is also present when the active convection portion of the MJO (i.e., phase 3 out of 4 based on Fig. 10 of the study) is moving eastward of the Maritime Continent (Chang et al., 2005). Thus, the MJO may inhibit weak cold surges since its circulation pattern directly opposes the north-easterly cold-surge winds. Additionally, the vortex is least likely to be present when the inactive convective portion of the MJO (i.e., phase 1 out of 4 based on Fig. 10 of the study) is over the Maritime Continent (Chang et al., 2005). Therefore, the frequency of cold surges and vortex days is reduced during periods when the MJO is present, and the overall relationship among the MJO, cold surges, and the Borneo vortex are complex.

Lim et al. (2017) also studied the impacts and interactions of cold surges and the MJO on rainfall over Southeast Asia. They found that the active phases of the MJO create a more favourable environment for convection by moistening the atmosphere, which in turn enhances

129 conditional instability. Although less frequent, cold surges that occur during the active phases of
130 the MJO result in higher rainfall, and the most extreme rainfall events reported by Lim et al. (2017)
131 occurred during these conditions. Additionally, Xavier et al. (2020) show that cross-equatorial
132 surges in February and March, which are characterised by prolonged periods of strong meridional
133 flow at the equator, tend to reverse the MJO wind fields and hence suppress the rainfall anomalies
134 in the northern parts of the western Maritime Continent. Cold surge advection from the
135 midlatitudes can also act as a thermodynamic barrier for the convection to develop in the southern
136 parts of the South China Sea in the presence of strong cross-equatorial surges.

137 This paper describes the synoptic structure and development of cold surges over the
138 Maritime Continent using observational and reanalysis datasets. Additionally, we analyse the
139 thermodynamics of the convection associated with cold surges from the perspective of plume
140 buoyancy. Section 2 outlines the data and methodologies used. Section 3 investigates the
141 climatologies of the seasonal and diurnal cycles of non-surge days, and dry, moderate, and wet
142 surges. Section 4 contrasts and discusses the synoptic structure of dry, moderate, or wet cold surges
143 using long-term composites. Section 5 analyses the relationship between the MJO, cold surges and
144 bursts in the Australian summer monsoon. Conclusions follow in Section 6.

145 **2 Data and Methods**

146 *2.1 ERA5 and GPM*

147 Output from the fifth reanalysis of the European Centre for Medium-Range Weather
148 Forecasts (ECMWF ERA5; Hersbach et al., 2019) is used to composite long-term observations
149 over a 20-year climatological period from November 2000 to March 2020 (NDJFM 2000-01 to
150 2019-20). The ERA5 data have a horizontal grid spacing of 0.25° x 0.25° and we use 27 vertical

151 levels from 1000 to 100 hPa. Daily averages of hourly resolution data are computed for the
152 following ERA5 fields: mean sea level pressure (MSLP), total column water vapour (TCWV),
153 zonal and meridional winds, vertical motion (ω), temperature, and specific humidity. The
154 temperature and specific humidity are also computed at 3-hourly intervals.

155 We use Global Precipitation Measurement (GPM; Huffman et al., 2019; National
156 Aeronautics and Space Administration [NASA], 2021) data to analyse the precipitation over the
157 same 20-year period. It has a horizontal grid spacing of 0.1° x 0.1° and the multi-satellite
158 precipitation estimate with gauge calibration field (i.e., 'precipitationCal') is used (Huffman et al.,
159 2019). The dataset containing the final estimate of daily accumulated GPM precipitation (i.e.,
160 GPM IMERG Final Precipitation L3) is used for the daily mean composites, and 30-minute
161 resolution data is used to analyse the diurnal cycle at 3-hourly intervals.

162 Finally, we use daily data for the MJO index over the entire climatological period, where
163 the real-time multivariate MJO index (RMM; Wheeler and Hendon., 2004) is used to identify the
164 amplitudes and phases of the MJO.

165 *2.2 Cold surge identification*

166 We identify cold surges by applying various criteria from Chang et al. (2005) and Lim et
167 al. (2017), as specified in Table 1.

168

*Table 1: Cold surge definition and criteria used in this study.*

| Variable | Condition |
|---|---|
| Mean sea level pressure (MSLP) | Exceed 1020 hPa anywhere within 18-22°N, 105-122°E (brown box in Figure 1). |
| 925 hPa wind speed | At least 0.75 standard deviations above the 20-year NDJFM mean when averaged over 5-10°N, 107-115°E (magenta box in Figure 1). |
| 925 hPa wind direction | Between 337.5° (north-north-westerly) and 90° (easterly). |

Based on the ERA5 climatology for NDJFM 2000-01 to 2019-20, the wind speed must be at least approximately 11.5 m $s^{-1}$ to satisfy the wind speed threshold. The cold surges must also satisfy the criteria for at least two consecutive days (Yihui, 1990). The advantage of using this cold surge identification method is that it eliminates weather systems with easterly flow from the Philippines, such as typhoons (Xavier et al., 2020). From these constraints in the wind speed and direction, only the 'South China Sea type' and 'Both type' of cold surge from Abdillah et al. (2021) are identified. These are also the only surge classifications that affect the Maritime Continent region. In total, the requirement for two consequtive surge days eliminates 40 single-day surges within the 20-year climatological period, leaving a total of 545 cold surge days and 132 surges that are two days or longer in duration.

### *2.3 Wet vs. dry cold surges*

Precipitation quartiles are used to distinguish between dry (below the lower quartile – 33 surges; 114 days), wet (above the upper quartile – 33 surges; 124 days), and moderate (between the quartiles – 66 surges; 307 days) cold surges for NDJFM 2000-01 to 2019-20. The precipitation thresholds for each category are based on precipitation averages over a domain encompassing Singapore and parts of Malaysia, Sumatra, and Borneo (see the "Precipitation domain", blue box in Figure 1). The boundary for the lower quartile is approximately 3.5 mm $d^{-1}$ and for the upper

quartile it is approximately 17.4 mm $d^{-1}$. Anomalies for each variable are calculated by subtracting the 31-day centred moving average seasonal cycle climatology. Composites over the 20-year climatology are used to analyse the synoptic-scale structure and development of cold surges, and the environments that characterise the dry, moderate, or wet surges. Lagged composites are computed between day -5 and day +5 relative to the surge onset for each cold surge category. Composite maps are plotted within 15°S–25°N, 95°E–125°E (see the dashed red box in Figure 1) and 5°S-20°S, 95°E-150°E for the Australian summer monsoon analysis (encompasses the "Australian monsoon domain", green box in Figure 1).

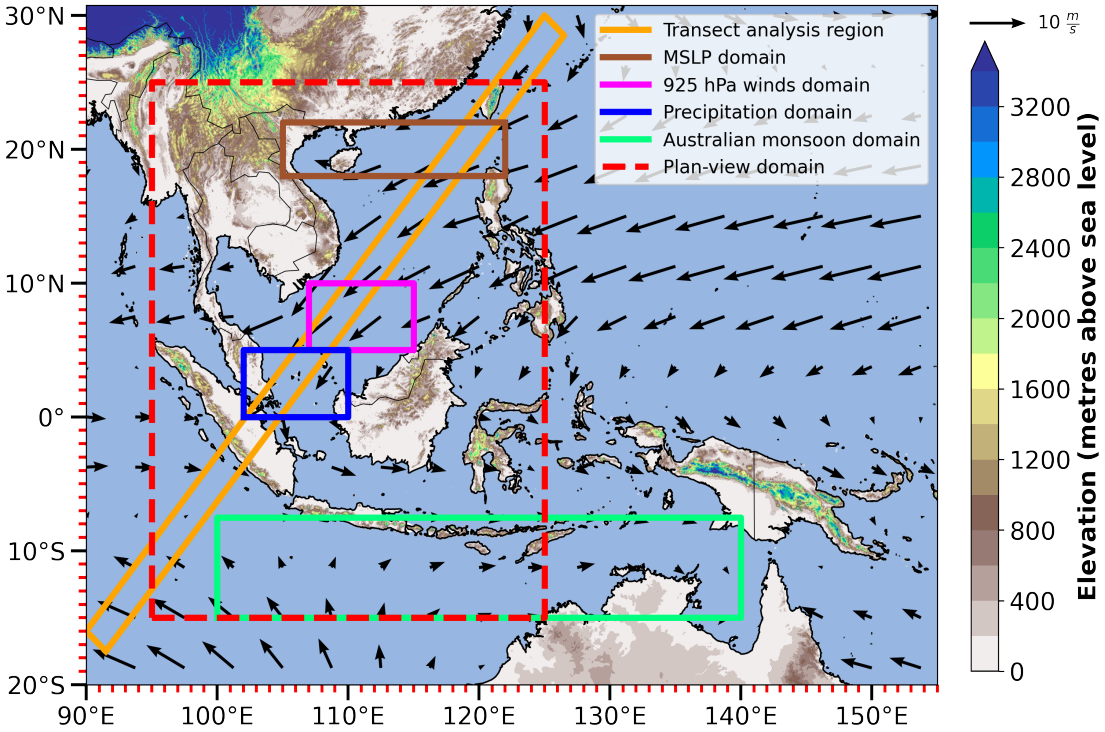


*Figure 1: Map of the Maritime Continent region that depicts the transect analysis region (orange box), the cold surge indices domains for MSLP (brown box) and 925 hPa winds (magenta box), the precipitation domain to contrast wet and dry cold surges (blue box), the composite maps analysis region (dashed red box), and the Australian monsoon domain (green box). 925 hPa wind vectors for the NDJFM 2000-01 to 2019-20 mean climatology.*

The relationship between cold surge days in each category and the MJO is also analysed. First, the RMM index (Wheeler & Hendon, 2004) is used to categorise days by phase of the MJO. Days with RMM amplitude greater than 1 are considered to be in one of phases 1 to 8 as defined

198 by the RMM index, otherwise the days are considered to be non-MJO days. For each surge type,
199 we then calculate the normalised frequency of days in each phase of the MJO. This is defined as
200 the fraction of days of a particular surge category that are in a particular phase of the MJO divided
201 by the fraction of all days in the climatology that are in the same phase of the MJO. For the
202 Maritime Continent, phases 2-4 are considered MJO active phases, while phases 5-7 are considered
203 MJO inactive phases.

204 *2.4 Plume buoyancy ($B_L$)*

205 We also analyse the thermodynamics of the convection associated with cold surges using
206 a diagnostic for the mid-tropospheric buoyancy experienced by an idealised entraining plume,
207 which we denote $B_L$. Similar diagnostics have been shown to closely relate to the onset of
208 convection over tropical regions in general (e.g., Gregory, 2001; de Rooy and Siebesma, 2010;
209 Ahmed and Neelin, 2018). Here we apply the formulation of Adames et al. (2021), in which $B_L$ is
210 defined:

211 $$B_L = \frac{g}{\kappa_L}\left(W_B \frac{\theta_{eB}-\theta^*_{eL}}{\theta^*_{eL}} - W_L \frac{\theta^*_{eL}-\theta_{eL}}{\theta^*_{eL}}\right) \qquad \text{(Eq. 1)}$$

212 where $$\kappa_L = 1 + \frac{L^2 q^*}{c_p R_v T^2} \ , \qquad \text{(Eq. 2)}$$

213 $$W_B = \frac{\Delta P_B}{\Delta P_L} ln(1 + \frac{\Delta P_L}{\Delta P_B}) \ , \qquad \text{(Eq. 3)}$$

214 and $$W_L = 1 - W_B \qquad \text{(Eq. 4)}$$

215 In Eq. 1, $g$ = 9.8 m s$^{-2}$, $\theta_{eB}$ and $\theta_{eL}$ denote the equivalent potential temperatures within the deep
216 boundary layer (DBL; 1000 to 850 hPa) and lower free troposphere (LFT; 850 to 600 hPa)
217 respectively, and $\theta^*_{eL}$ is the saturation equivalent potential temperature within the LFT. In Eq. 2,
218 $\kappa_L$ is the scaling term, where $L$ = 2.5 x 10$^6$ J kg$^{-1}$ K$^{-1}$ is the latent heat of vaporisation, $c_p$ = 1004 J
219 kg$^{-1}$ K$^{-1}$ is the specific capacity of dry air, $R_v$ = 461 J kg$^{-1}$ K$^{-1}$ is the gas constant of water vapour,

220 $q^*$ is the saturation specific humidity, and $T$ is the temperature. In Eq. 3 and 4, $\Delta P_B$ and $\Delta P_L$ denote
221 the pressure thickness of the DBL and LFT (150 and 250 hPa) respectively.

222 While buoyancy is defined using temperature or potential temperature (θ), $B_L$ is defined in
223 terms of equivalent potential temperature ($\theta_e$) because it is approximately conserved during moist
224 adiabatic processes. Adames et al. (2021) nevertheless interpret $B_L$ as a measure of the buoyancy
225 of an air parcel as it rises to the top of the LFT layer, mixing with its environment. We may
226 therefore see $B_L$ as a measure of convective instability of the lower troposphere that accounts for
227 the effects of mixing. In particular, we note that there are two terms in Eq. 1, each given a weighting
228 $W_B$ or $W_L$. The first term is the 'undilute $B_L$', which is a traditional measure of the convective
229 instability of the lower troposphere (Raymond et al., 2015; Adames et al., 2021). For this measure
230 of convective instability, the parcel is assumed not to mix as it passes through the LFT. Positive
231 values of undilute $B_L$ indicate unstable profiles with a high potential for convection, provided air
232 is lifted from the boundary layer (i.e., the DBL at 850 hPa) without mixing with its environment.
233 The second term is a function of the saturation deficit of the LFT, and it represents the reduction
234 in buoyancy in a rising plume as it entrains and is diluted by free-tropospheric air. The importance
235 of the second term is set by the weights $W_B$ and $W_L$, which describe the relative mass inflow to the
236 plume from the DBL and LFT. For the parameters used here (taken from Adames et al. 2021), $W_B$
237 = 0.59 and $W_L$ = 0.41.

238 As $B_L$ increases from negative values towards zero, Adames et al. (2021) show that
239 precipitation increases exponentially (see their Fig. 3). They also note a critical value of $B_L \sim$ -0.02
240 m $s^{-2}$ that marks the beginning of the transition to a linear precipitation regime, where precipitation
241 increases linearly and rapidly with increasing values of $B_L$. Although $B_L$ is averaged between 15°N

and 15°S in the Adames et al. (2021) study, here we compute $B_L$ over the precipitation domain and the composite maps analysis region (see the blue and dashed red boxes respectively in Figure 1).

## 3 Climatologies of the Seasonal and Diurnal Cycles

### *3.1 Seasonal cycle of wet and dry cold surges*

There is a clear seasonal cycle in GPM precipitation, which is averaged over the precipitation domain and during NDJFM. The 31-day centred moving average precipitation peaks at approximately 11.5 mm $d^{-1}$ in the middle of December, and is lowest at approximately 4.1 mm $d^{-1}$ in early March (Figure 2a). Most wet surge days are also found in December and January (57 and 42 days respectively) and most dry surge days are found in January and February (39 and 54 days respectively; Figure 2b).

Overall, cold surge days contribute approximately 30% of total rainfall within the 20-year climatological period (545 surge days out of 3025 days, or approximately 18%), where close to half of the surge rainfall contribution occurs in each of the wet and moderate surge days (approximately 14.7% and 14.3% respectively), and less than 1% in the dry surge days (Figure 2c). The higher contribution of rainfall from cold surges relative to the fraction of cold surge days within the 20-year period is explained by the overall higher daily mean rainfall rate during cold surge days (approximately 12.3 mm $d^{-1}$ for all cold surge days and 10.5 mm $d^{-1}$ for moderate surges) than non-surge days (approximately 6.4 mm $d^{-1}$; Figure 2d). Dry and wet surges also have a daily mean rainfall rate of approximately 1.7 mm $d^{-1}$ and 26.6 mm $d^{-1}$ respectively. When the seasonal cycle is removed, there are individual days within the wet surge category that fall below the climatological mean (20 out of 124 days) and vice versa for dry surges (7 out of 114 days). This is expected since the precipitation quartiles for each surge category are based on the mean precipitation of entire cold surges rather than individual cold surge days.

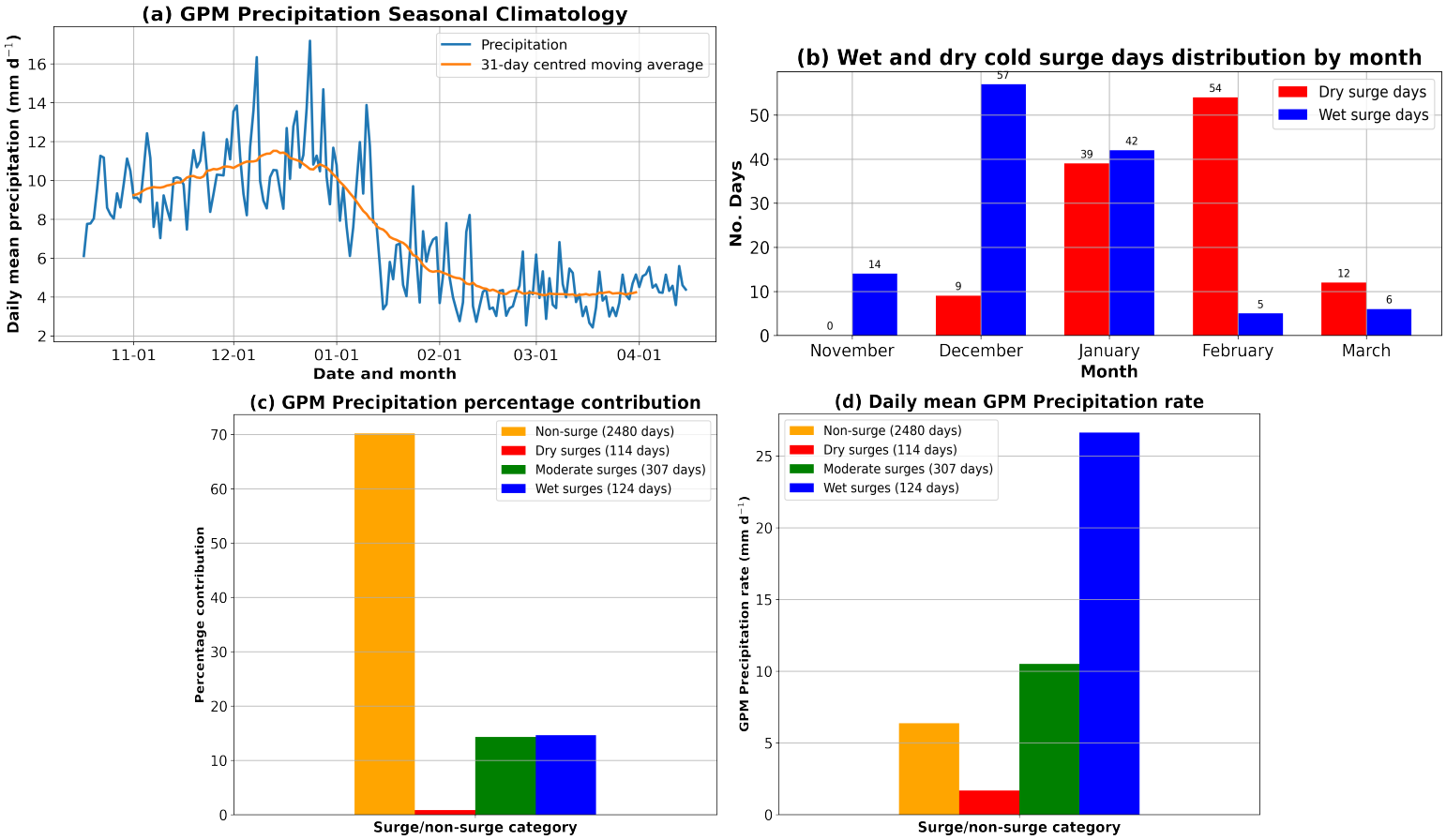


*Figure 2: (a) Seasonal cycle of daily GPM precipitation from 1 November to 31 March (blue lines) with 31-day centred moving average curves (orange lines) averaged over 2000-01 to 2019-20. (b) Distribution of dry (red bars) and wet (blue bars) cold surge days by month over the NDJFM season. (c) GPM precipitation percentage contribution and (d) daily mean GPM precipitation rates. Non-surge days (orange), and dry (red), moderate (green), and wet (blue) cold surge days.*

### *3.2 Diurnal cycle of plume buoyancy and GPM precipitation*

There is a clear relationship between daily mean values of $B_L$ and GPM precipitation averaged over the precipitation domain on individual days within the 20-year period for non-surge days and each of the three surge categories (Figure 3a). Most wet surge days (119 out of 124 days) exceed the -0.02 m $s^{-2}$ threshold for $B_L$ while most dry surge days fall below the threshold (94 out of 114 days). Overall, the cold surge days are closer to the threshold, but this may be simply due to the smaller sample size (545 days) compared to non-surge days (2480 days).

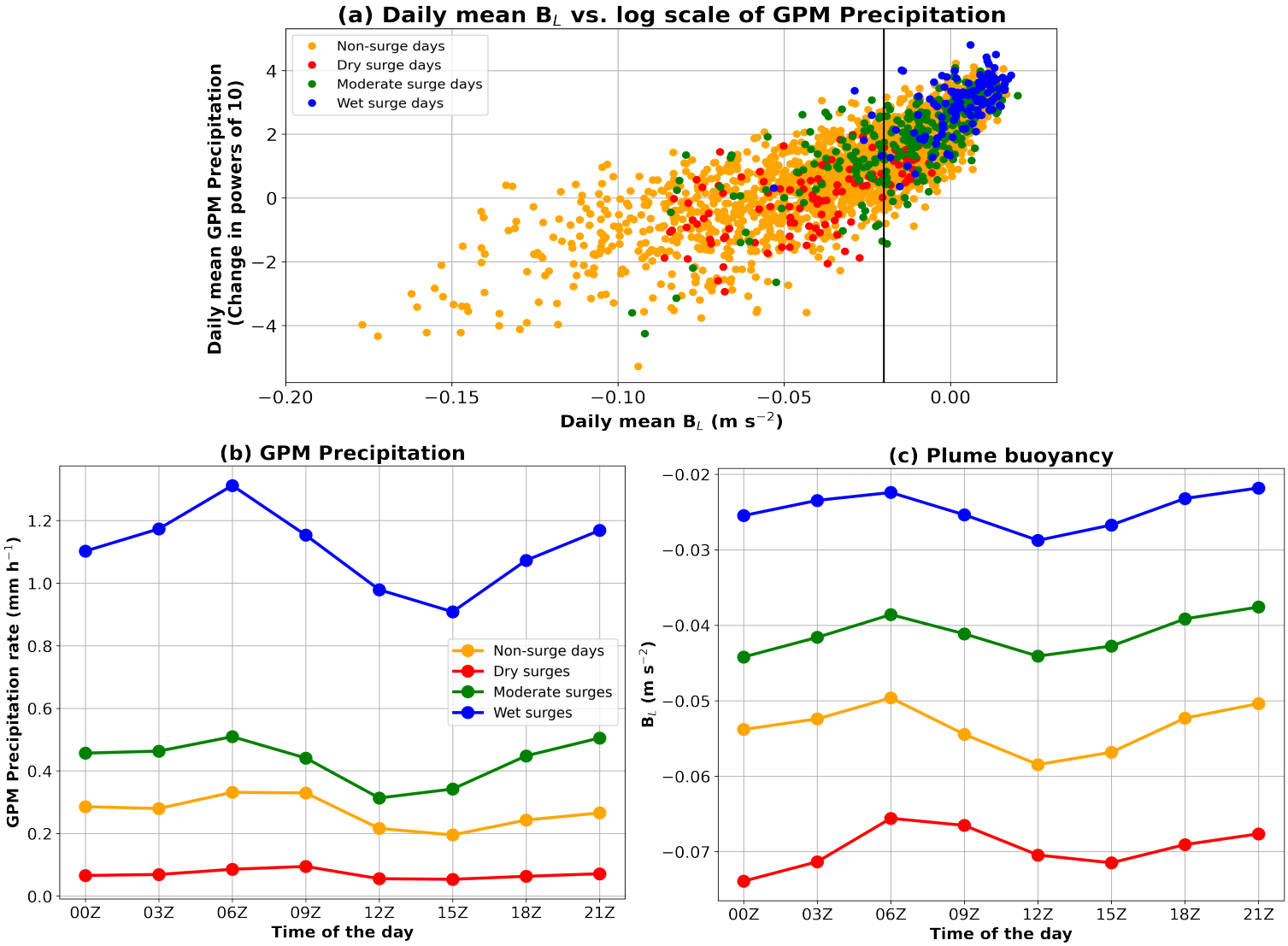


*Figure 3: (a) Daily mean $B_L$ vs. log scale of GPM precipitation over the precipitation domain in NDJFM 2000-01 to 2019-20. Non-surge days (orange), and dry (red), moderate (green), and wet (blue) cold surge days. The vertical black line is drawn at the -0.02 m $s^{-2}$ threshold for $B_L$. Diurnal cycle of mean (b) GPM precipitation rate and (c) $B_L$. Non-surge days (orange), and dry (red), moderate (green), and wet (blue) cold surge composites.*

In terms of the diurnal cycle, both the hourly precipitation rate (Figure 3b) and $B_L$ (Figure 3c) over the precipitation domain are highest in the wet surge composites, followed by the moderate, non-surge, and dry composites. In the wet and moderate surge composites, GPM precipitation peaks at 06Z (14:00 LST; approximately 1.31 and 0.509 mm $h^{-1}$ respectively) and the diurnal contrasts are more pronounced. Precipitation rates at 21Z (05:00 LST) for the wet and dry composites (approximately 1.17 and 0.505 mm $h^{-1}$ respectively) are also well above the daily mean

values (approximately 1.11 and 0.44 mm $h^{-1}$ respectively), and closer to the 06Z (14:00 LST) peak compared to the non-surge and dry surge composites, which is most likely because of offshore precipitation during the nocturnal hours. The precipitation rate peaks between 06Z and 09Z (14:00 LST and 17:00 LST) in the non-surge composites (approximately 0.33 mm $h^{-1}$), and 09Z (17:00 LST) in the dry surge composites (approximately 0.09 mm $h^{-1}$). On the other hand, troughs in the diurnal cycle occur at 15Z (23:00 LST) for both the wet surge and non-surge composites (approximately 0.91 and 0.20 mm $h^{-1}$ respectively), between 12Z and 15Z (20:00 LST and 23:00 LST) in the dry (approximately 0.05 mm $h^{-1}$), and 12Z (20:00 LST) in the moderate surge composites (approximately 0.31 mm $h^{-1}$). In contrast, there is a daytime peak of $B_L$ at 06Z (14:00 LST) in all cases, and a greater peak at 21Z (05:00 LST) in the wet and moderate surge composites (approximately -0.022 and -0.038 m $s^{-2}$ respectively) since nocturnal convection occurs over the ocean in these cases. Nocturnal troughs are observed at 12Z (20:00 LST) for all categories but 15Z (23:00 LST) in the dry surge composites, and a lower minimum at 00Z (08:00 LST) for the dry and moderate composites (approximately -0.074 and -0.044 m $s^{-2}$ respectively).

Given the timings of peaks and troughs for both GPM precipitation and $B_L$ in Figures 3b and 3c, we compare their spatial distribution for the dry and wet surge composites by averaging over 06Z and 09Z (14:00 LST and 17:00 LST) for the daytime average (Figures 4a, c, e, g), and 18Z and 21Z (02:00 LST and 05:00 LST for the nocturnal average (Figures 4b, d, f, h). The diurnal cycles are compared on day +1 relative to surge onset, which is when the cold surge reaches its peak over the precipitation domain and most of the South China Sea. In both the dry and wet surge composites, wet anomalies are generally observed over land areas during the daytime average (Figures 4a, c), and over the surrounding ocean during the nocturnal average (Figures 4b, d) due to the offshore propagation of precipitation at night. The diurnal cycle of precipitation is strongest

over Sumatra, Java, and Sulawesi island. In the distribution of $B_L$ (Figures 4e, f, g, h), the diurnal cycle is clearest over Java, where areas which exceed the -0.02 m $s^{-2}$ threshold are consistent with areas of strongly enhanced (exceeding 1 mm $h^{-1}$) wet anomalies during the daytime average (Figures 4e, g).

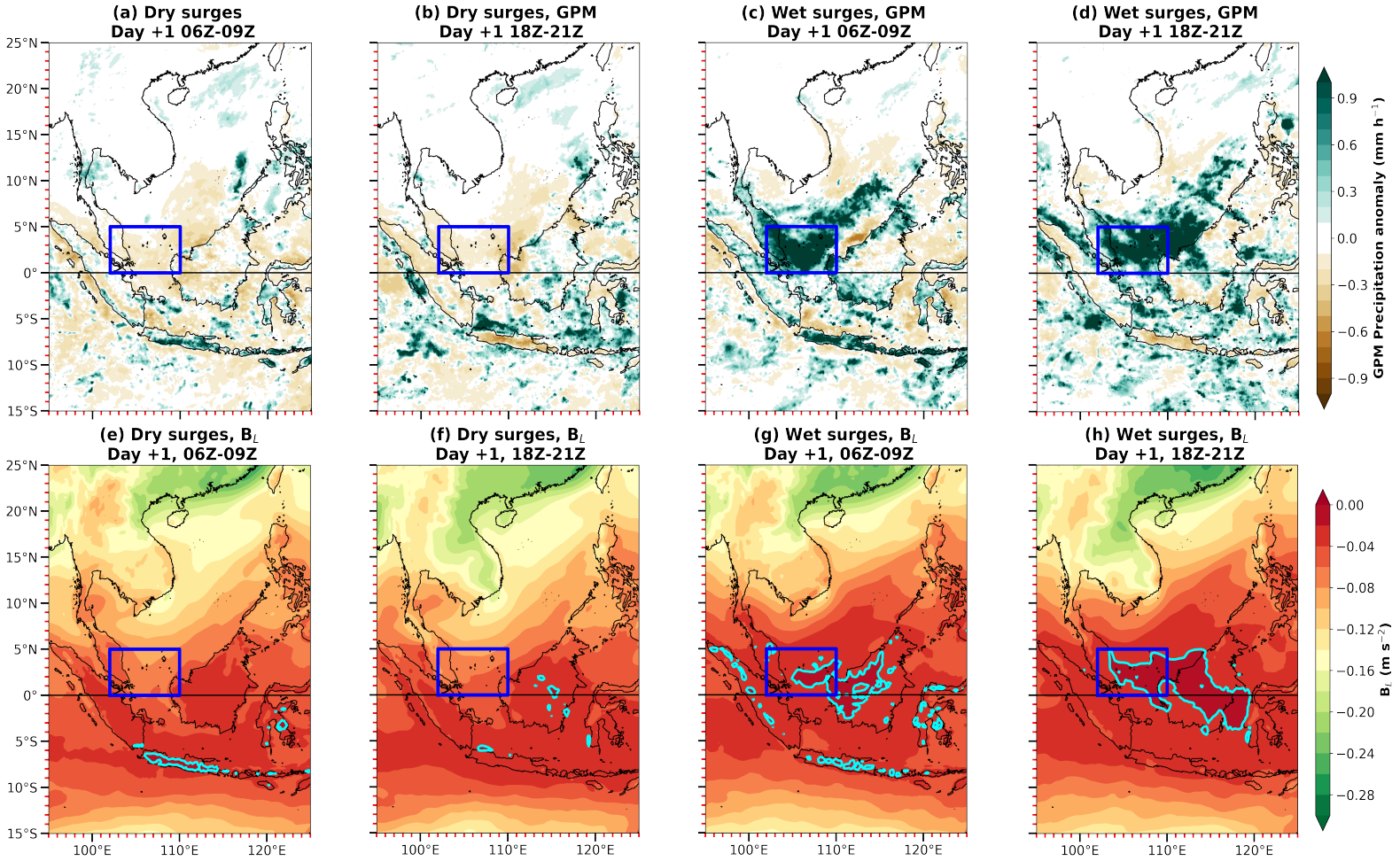


*Figure 4: Composite maps of (a-d) GPM precipitation anomalies with the seasonal cycle removed, and (e-h) layer average (850-600 hPa) values of $B_L$. Averages taken over 06Z and 09Z (a, c, e, g), and 18Z and 21Z (b, d, f, h). Dry and wet cold surges on day +1 relative to surge onset. The precipitation domain is depicted by the blue box. The cyan contours indicate the -0.02 m $s^{-2}$ threshold for the $B_L$ linear precipitation regime described in Adames et al. (2021).*

Over the precipitation domain, the diurnal cycle is suppressed. Dry anomalies (-0.1 to -0.4 mm $h^{-1}$) are observed in the dry surge composites due to the propagation of colder and drier surge air from the northern South China Sea. Strongly enhanced wet anomalies are observed over much of the domain and equatorial South China Sea in the wet surge composites, regardless of the time

of day. For the wet composites, there is a land-ocean contrast along the north-west coast of Borneo between the daytime and nocturnal average. The strongly enhanced wet anomalies are more widespread during the nocturnal average over this region, which is consistent with the large area where $B_L$ exceeds the threshold value in Figure 4h.

Overall, $B_L$ distinguishes the three classes of cold surges well, implying that wet surges are characterised by a moister free troposphere, which allows convection to penetrate through the lower troposphere. This implication will be further investigated in the lagged composite analysis of TCWV and 700 hPa ω anomalies in the next section.

## 4 Synoptic Structure of Cold Surges

### *4.1 The development of cold surges over the Maritime Continent*

In this section, we investigate the synoptic environments of each cold surge category using lagged composite anomalies of TCWV (Figure 5), and ω at 700 hPa (not shown). The 925 hPa wind anomaly vectors are also shown on each map.

The strength of the north-easterly surge wind anomalies is similar in the three surge categories, although their characteristics near the equator differ in the day +1 maps. The dry surge composites are characterised by cross-equatorial flow that reaches equatorward to Java, with westerly anomalies around Java (Figure 5d). In contrast, the wet surge composites coincide with a cyclonic circulation between Borneo and the Malaysian Peninsula instead of cross-equatorial flow (Figure 5e). The moderate surge composites depict weaker cross-equatorial flow and westerly anomalies over Java compared to the dry surge composites (Figure 5f).

Negative TCWV anomalies from the cold surge extend to the equator in the dry surge composites (-1 to -5 mm), transitioning to weak positive anomalies around Java (+1 to +2 mm; Figures 5a, d). These negative anomalies cover almost the entire precipitation domain and most of

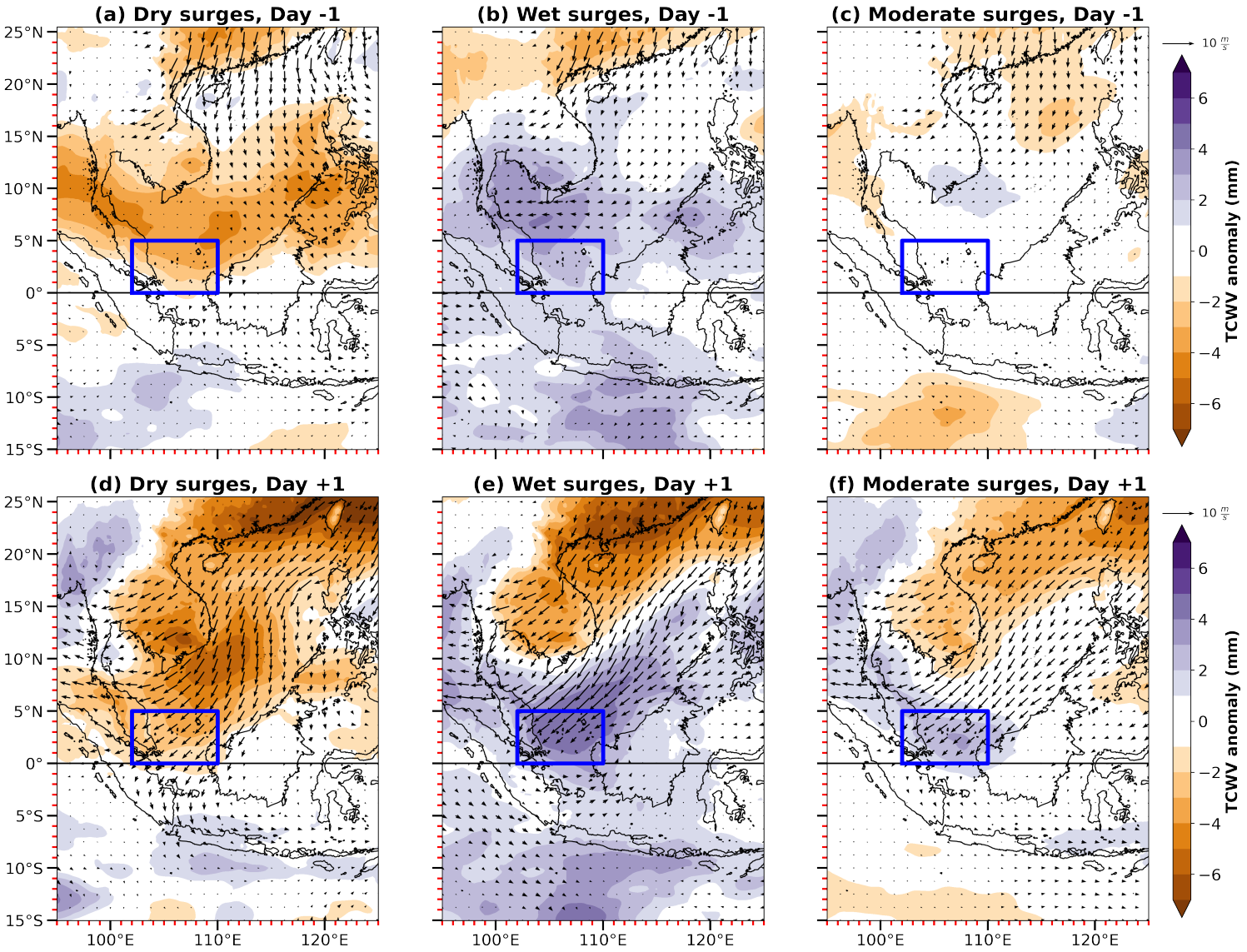


*Figure 5: Lagged composite maps of daily mean TCWV anomalies with the seasonal cycle removed. Daily mean 925 hPa horizontal wind anomaly vectors. (a, d) Dry, (b, e) wet, and (c, f) moderate cold surges on day -1 (top row) and day +1 (bottom row) relative to surge onset. The precipitation domain is depicted by the blue box.*

the South China Sea by day -1. The dry anomalies strengthen and peak under -7 mm to the northeast of Taiwan on day +1 as the cold surge reaches its peak, while the strengthening cross-equatorial flow coincides with the positive anomalies over Java. In the wet surge composites (Figures 5b, e), widespread positive TCWV anomalies are already evident prior to surge onset (+2 to +4 mm). A meridional TCWV anomaly gradient is found on day +1, ranging from over +4 mm over the equator to -6 mm over the northern South China Sea. This sharp gradient is consistent

with the convection near the equator in contrast to drier surge air over the northern South China Sea. Weaker TCWV anomalies are observed in the moderate surge composites on day -1 over the precipitation domain and much of the South China Sea (-2 to +1 mm; Figure 5c). On day +1 (Figure 5f), the anomalies follow a similar pattern to that of the wet surge composites, although the meridional moisture gradient is weaker, ranging from +3 mm at the equator to -5 mm over the northern South China Sea.

In each cold surge category, dry air from the surge is accompanied by positive 700 hPa ω anomalies (i.e., stronger descent or weaker ascent relative to climatology), particularly on day +1. Positive anomalies associated with the surge over Southern China are most widespread in the dry surge composites (peaking close to 0.10 Pa $s^{-1}$), and weaker anomalies are observed over most of the South China Sea (+0.00 to +0.03 Pa $s^{-1}$). These positive anomalies strengthen between day -1 and day +1, and negative anomalies strengthen around Java (-0.01 to -0.06 Pa $s^{-1}$ over most parts). It is likely that both the lack of moisture from negative TCWV anomalies and lack of ascent around the equatorial South China Sea in the dry surge composites enable dry air to be advected towards the equatorial latitudes. From day -1, areas of enhanced ascent are already evident over much of the equatorial South China Sea in the wet surge composites (-0.01 to -0.06 Pa $s^{-1}$). Large areas of strongly enhanced ascent develop and strengthen by day +1 (under -0.10 Pa $s^{-1}$ over much of the precipitation domain), which is consistent with GPM precipitation anomaly patterns from Figures 4c, d. In the moderate surge composites, the 700 hPa ω anomalies are relatively weak over the precipitation domain on day -1 (-0.03 to +0.03 Pa $s^{-1}$). The anomaly patterns also follow a similar structure to the wet surge composites from day +1, with enhanced ascent over the precipitation domain (peaking close to -0.10 Pa $s^{-1}$).

Cold surges over the northern South China Sea are characterised by below average moisture, and enhanced descent. In the dry surge composites, the stronger descent or weaker ascent, and dry air reach the precipitation domain, whereas relatively moist air ascent and enhanced ascent is found over the Java area. Enhanced ascent over the precipitation domain and the strong meridional TCWV anomaly gradient explain the strongly enhanced precipitation anomalies in the wet surge composites. These results are consistent with the GPM precipitation anomaly and $B_L$ results.

*4.2 Transect analysis of cold surges*

ERA5 data are also averaged over 7 transects that are spaced at 0.25° along the South China Sea (see the "Transect analysis region", orange box in Figure 1). Nearest-neighbour interpolation is performed for each variable along each transect at the same horizontal resolution. The north-easterly component of the 925 hPa along-transect wind anomalies depict a rapid acceleration of negative anomalies towards the equator in cold surges from about day -2 (Figure 6a). Wind anomalies peak under -5 m $s^{-1}$ on day +1 when the surge is strongest. $\theta_e$ anomalies at 925 hPa are also an indicator of both temperature and moisture anomalies (Figure 6b). Overall, negative 925 hPa $\theta_e$ anomalies (i.e., cold and dry anomalies; peaking at approximately -9 K), which are likely associated with the Siberian high outflow, are advected much slower towards the equator (approximately 5 m $s^{-1}$) compared to the propagation of north-easterly winds (approximately 30 m $s^{-1}$). This finding is consistent with the Rossby adjustment problem on the beta plane by Lim and Chang (1981), where the establishment of the Rossby wave group from the Siberian high explains the development of the north-easterly wind flow. Chang et al. (1983) takes the theoretical framework of Lim and Chang (1981) further to show that cold surges occurred in two distinct stages. The first stage was characterised by a significant rise in surface pressure at the cold surge

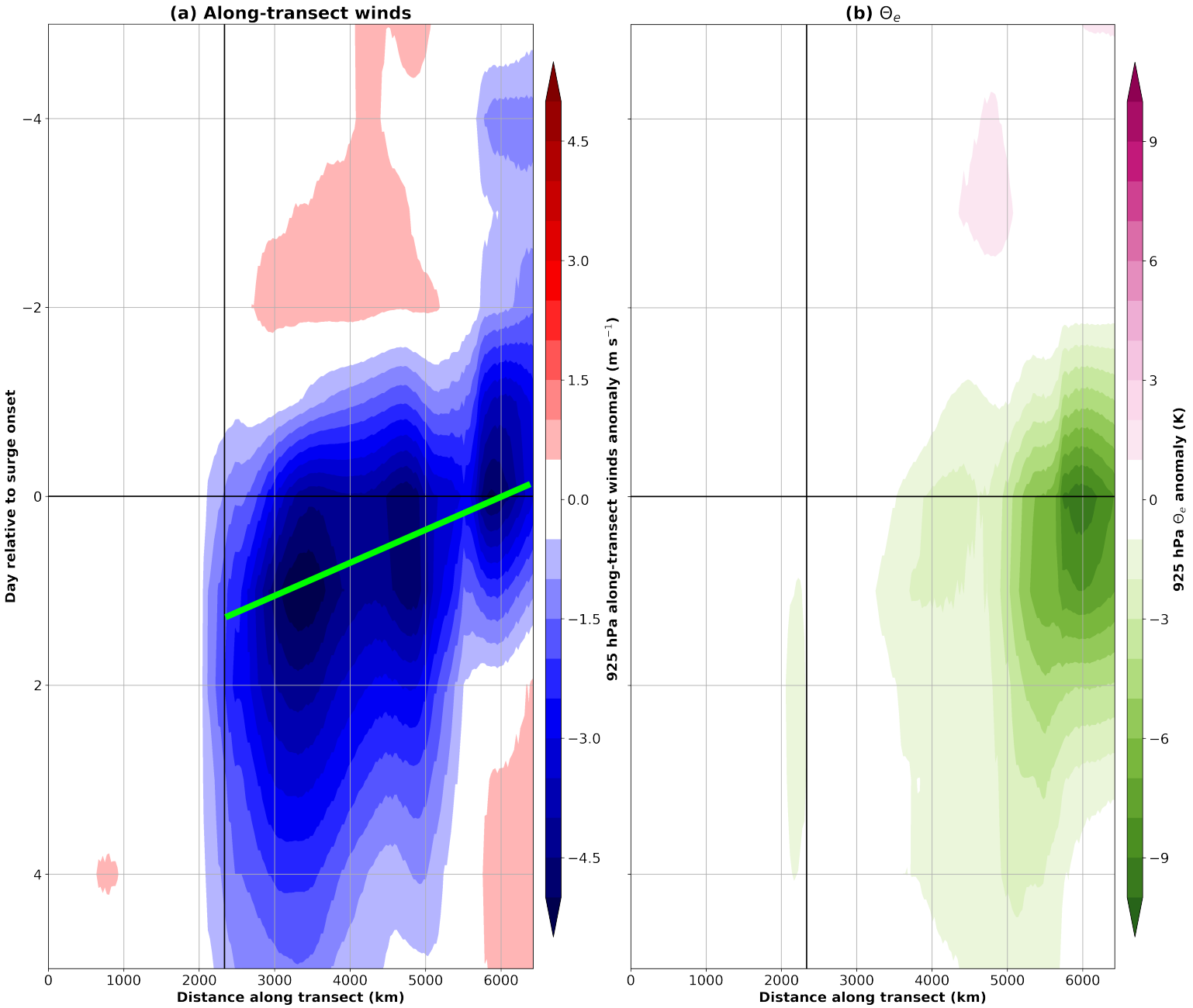


*Figure 6: Lagged composite plots of transect-averaged daily mean anomalies of 925 hPa (a) along-transect winds and (b) $\theta_e$ from day -5 to day +5 relative to surge onset with the seasonal cycle removed. The mean of all 545 cold surge days is taken. The transects are averaged over the orange box in Figure 1. The approximate location of the equator is marked by the vertical black line, and the transects are constructed from south-west to north-east moving left to right. Along-transect winds are negative moving north-east to south-west. The green line indicates the approximate speed of the north-easterly surge wind propagation.*

383 'edge' and gravity-wave type motions associated with equatorial propagation at about 40 m s$^{-1}$,

384 and the second stage featured a sharp decrease in surface dew point temperature accompanied by

a decrease in surface temperature that were associated with a cold front passage. Following both stages was a strengthening of the surface wind, often with a northerly acceleration (Chang et al., 1979, 1983). Therefore, the propagation of the surge may be viewed as a transient motion under the adjustment of the pressure-wind imbalance. This explains the faster propagation speed of north-easterly winds relative to the slower advection velocity of negative 925 hPa $\theta_e$ anomalies in our cold surge composites.

The vertical structure of the $\theta_e$ anomalies are then compared for the dry, wet, and moderate cold surge composites from 1000 to 100 hPa (Figure 7). We include vectors for the magnitudes of along-transect winds and $\omega$ to show areas of convergence and divergence, and ascent and descent, respectively. $\omega$ is also exaggerated by a factor of 50. In all cases, descent and negative $\theta_e$ anomalies deepen and strengthen between day -1 and day +1, strongest within the lower troposphere (approximately 1000 to 750 hPa) and in the dry surge composites (under -7 K; Figures 7a, d). Towards the north-eastern end of the transect, north-easterly winds also extend from the surface to approximately 700 hPa before shifting to south-westerly aloft.

Areas of convergence and uplift at the lower levels (with divergence towards the upper troposphere) correspond to positive low-level $\theta_e$ anomalies and enhanced precipitation anomalies. Descent and negative $\theta_e$ anomalies are associated with negative precipitation anomalies. Cold and dry anomalies are already observed on day -1 over most of the South China Sea in the dry surge composites (-1 to -3 K; Figure 7a). Warm and moist anomalies are observed in the wet surge composites approximately between the equator and 12°N (+1 to +2 K; Figure 7b). In both cases the anomalies extend from approximately 900 to 450 hPa. On day +1 in the wet composites, positive $\theta_e$ anomalies become more widespread along the South China Sea, and increase with height from the surface (0 to -1 K) to approximately 800 hPa (+1 to +3 K; Figure 7e). Precipitation

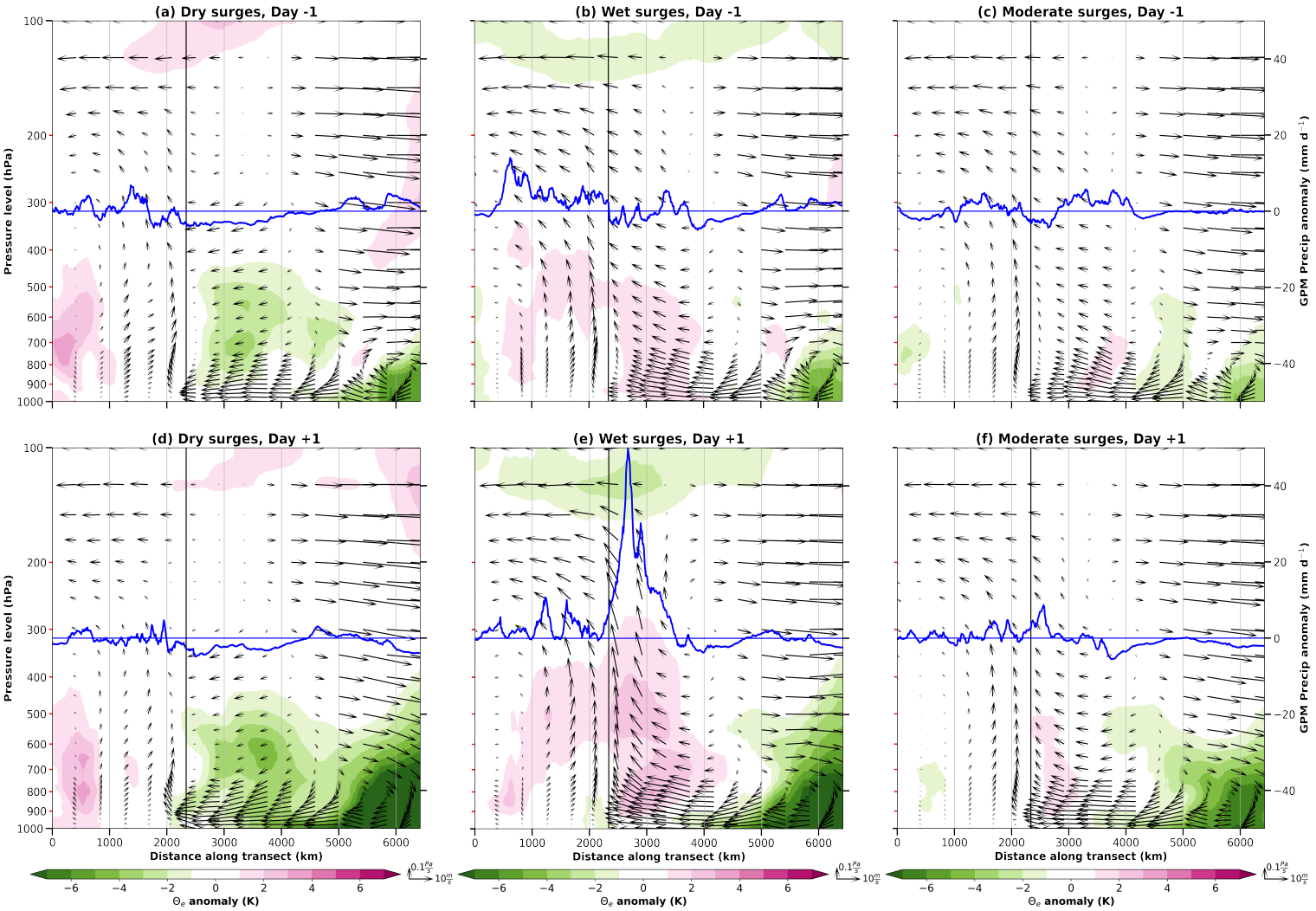


*Figure 7: Lagged composite plots of transect-averaged daily mean ERA5 $\theta_e$ anomalies from 1000 to 100 hPa (contours) and daily mean GPM precipitation anomalies (blue lines) with the seasonal cycle removed. (a, d) Dry, (b, e) wet, and (c, f) moderate cold surges on day -1 (top row) and day +1 (bottom row) relative to surge onset. The wind vectors represent the magnitudes of daily mean along-transect winds and ω. ω is exaggerated by a factor of 50. The transects are averaged over the orange box in Figure 1. The approximate location of the equator is marked by the vertical black line, and the transects are constructed from south-west to north-east moving left to right.*

anomalies are highest (peaking at approximately +45 mm $d^{-1}$) just to the north of the equator where positive $\theta_e$ anomalies and ascent are strongest. This vertical gradient in $\theta_e$ anomalies means that the lowest layers of the atmosphere are potentially stable. In the moderate surge composites (Figure 7c, f), both the cold and dry anomalies from the surge (up to -7 K at the northeastern end of the transect), and warm and moist anomalies (0 to +1 K) near the equator follow a similar pattern to that of the wet surge composites. Finally, the extent of cross-equatorial flow is greatest in the dry

surge composites and least in the wet surge composites, which is consistent with wind patterns in Figure 5.

## 5 Cold surges, MJO, and Australian summer monsoon bursts

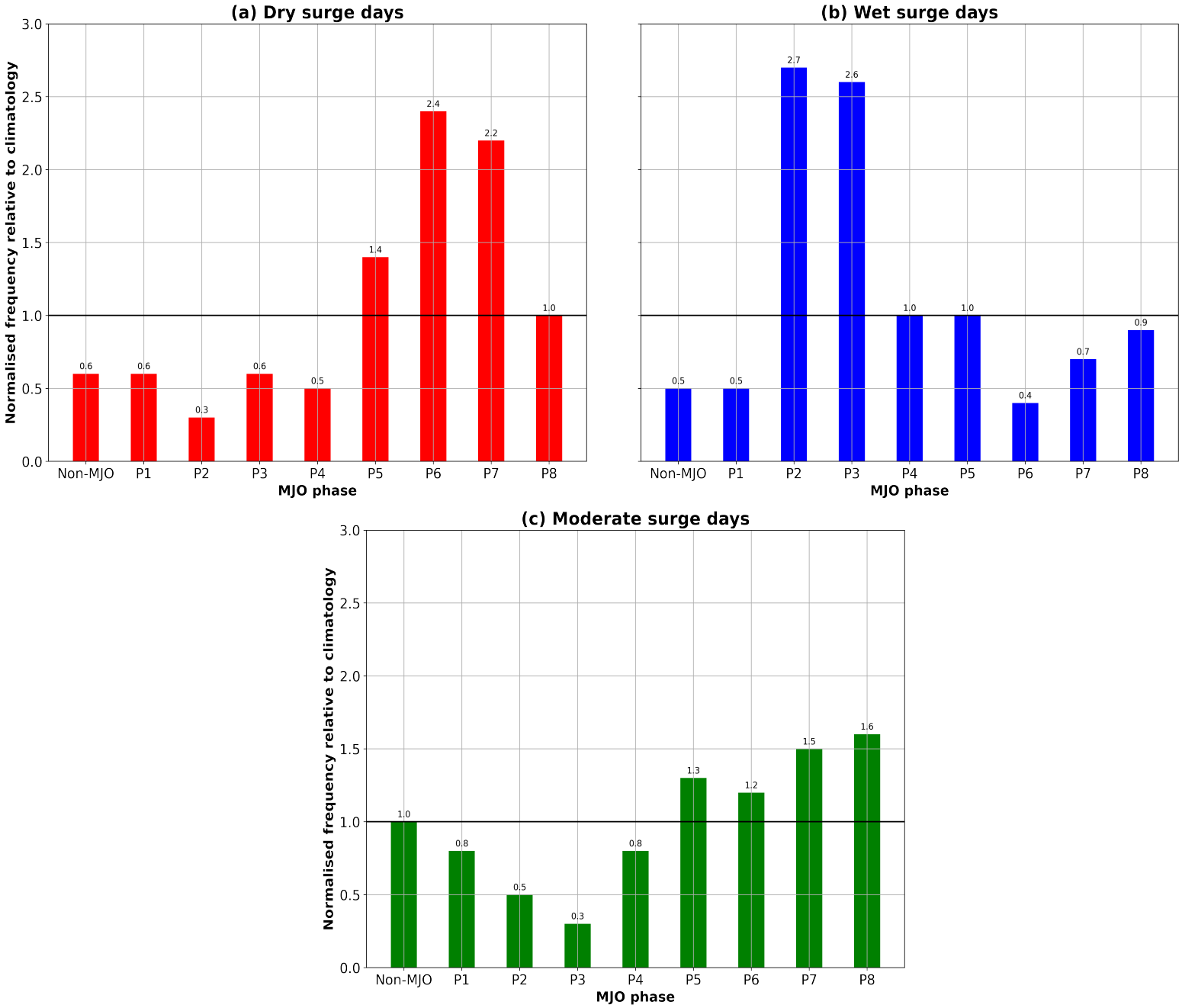


*Figure 8: Normalised frequency for phases of the MJO (including non-MJO days) relative to climatology. (a) Dry, (b) wet, and (c) moderate cold surge days. The horizontal black line is drawn at a normalised frequency of 1.0, where the percentage occurrence of a particular phase of the MJO is equal to that of climatology.*

417 Figure 8 shows the normalised frequency of cold surge days in each phase of the MJO
418 (including non-MJO days) relative to climatology for the three surge categories. There is a clear
419 correlation between the phase of the MJO and the number of dry or wet surge days, although the
420 presence of a surge in each category is not uniquely tied to particular phases of the MJO. Dry surge
421 days have normalised frequencies that peak at approximately 2.4 and 2.2 in phases 6 and 7
422 respectively (Figure 8a), whereas wet surge days have peaks at approximately 2.7 and 2.6 in phases
423 2 and 3 respectively (Figure 8b). For moderate surge days (Figure 8c), the normalised frequency
424 is lowest in phase 3 (approximately 0.3) and highest in phase 8 (approximately 1.6). Here, the
425 frequency of the active phases is reduced while that of the suppressed phases is increased. In phases
426 5-8, the normalized frequencies are all greater than 1. These findings agree with the Chang et al.
427 (2005) and Lim et al. (2017) studies which reported southwesterly anomalies over a large area of
428 East Asia and western Pacific during phases 2 and 3. According to Lim et al. (2017), these
429 anomalies are consistent with the Rossby wave response to the MJO convection pattern, which
430 partially counter the north-easterly cold surge winds.

431 To better understand the influence of the MJO on cold surges, composites of daily mean
432 MSLP anomalies (Figures 9a-d) and GPM precipitation anomalies (Figures 9e-h) are shown in
433 the active phases for the wet surge composites and suppressed phases for the dry composites. The
434 non-dominant or non-MJO phases are also compared for both categories. The same analysis is
435 conducted over the Australian monsoon domain (see the green box in Figure 1; Figures 15 and
436 16). Based on Figure 8, phases 5-7 are composited for the dry surges and phases 2-3 for the wet
437 surges. Another set of composites are taken for all other phases of the MJO and non-MJO days to
438 expose the effect of removing the dominant MJO signal. In all cases, the north-easterly wind
439 anomalies from the cold surge are consistently associated with positive MSLP anomalies, which

are strongest at the northernmost part of the region over inland Southern China (peaking over +5.0 hPa in the dry surge composites).

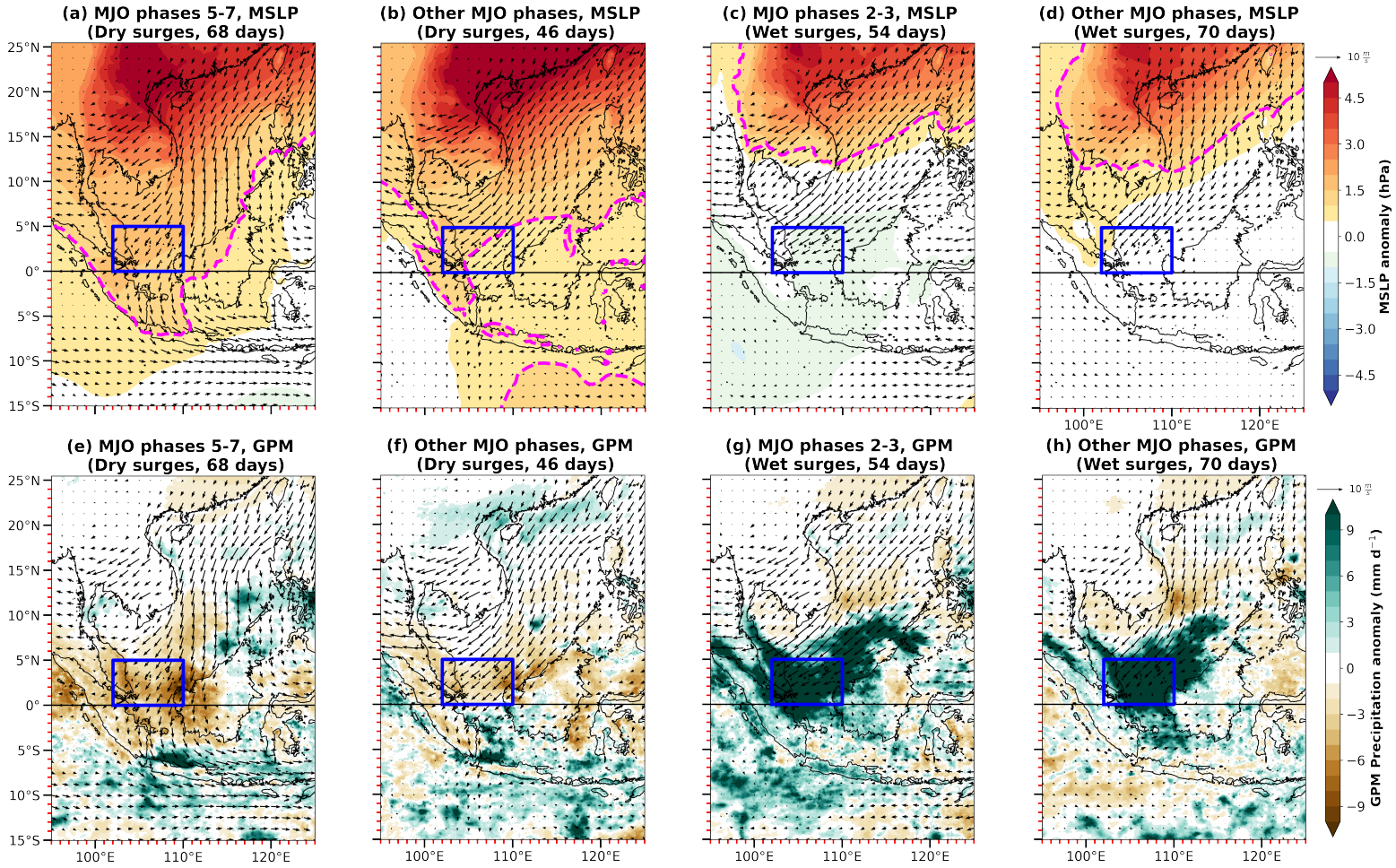


*Figure 9: Composite maps of daily mean (a-d) MSLP anomalies and (e-h) GPM precipitation anomalies (bottom) with the seasonal cycle removed. Daily mean 925 hPa horizontal wind anomaly vectors. Dry and wet cold surges in both the dominant phases of the MJO (a, c, e, g), and all other phases including non-MJO days (b, d, f, h). The precipitation domain is depicted by the blue box. The dashed pink line on the MSLP plots represents the +1.0 hPa MSLP anomaly.*

In the dry surge composites, the +1.0 hPa MSLP anomalies cross the equator and extend to Java, as with the cross-equatorial wind flow. These circulation patterns are characteristic of the 'Both type' surges in Abdillah et al. (2021). Westerly anomalies are widespread over Java in phases 5-7 of the MJO along with weak low-pressure anomalies to the south-east of the domain (-0.5 hPa; Figure 9a). Widespread high-pressure anomalies are observed outside these suppressed phases of the MJO, with no westerly anomalies over Java (Figure 9b). In both cases, an inverse

448 relationship in rainfall is found with negative precipitation anomalies (peaking close to -10 mm d-
449 [1] in the suppressed phases of the MJO) over the precipitation domain and strongly enhanced
450 precipitation anomalies (peaking over +10 mm $d^{-1}$) off the north-west coast of Java. The
451 precipitation gradients are stronger in the suppressed phases of the MJO. On the other hand, the
452 +1.0 hPa contour in the wet surge composites is confined to above 10°N, which is characteristic
453 of the 'South China Sea type' surge in Abdillah et al. (2021). Positive MSLP anomalies extend
454 further equatorward outside the active phases of the MJO (Figure 9d). In contrast, the active phases
455 coincide with weak low pressure anomalies (-0.5 to -1.0 hPa) over most of the precipitation
456 domain, Java, and the Indian Ocean (Figure 9c). In both cases, a cyclonic circulation is evident
457 around Borneo, which corresponds to the large area of strongly enhanced precipitation anomalies
458 over the equatorial South China Sea. There are also patches of dry anomalies (-1 to -7 mm $d^{-1}$)
459 further north along the South China Sea and no strongly enhanced precipitation anomalies over
460 the Java region unlike the dry surge composites.

461 Over the Australian monsoon domain, the widespread westerly anomalies in phases 5-7 of
462 the MJO for the dry surge composites are associated with a strong north-west to south-east pressure
463 gradient between Java and northern Australia (Figure 10a). Low pressure anomalies just off the
464 north-west coast of northern Australia and at the southern end of the domain peak just under -1.0
465 hPa. In contrast, the wet surge composites in phases 2-3 of the MJO depict a reversed pressure
466 gradient associated with easterly anomalies, with widespread high pressure anomalies exceeding
467 +1.0 hPa over much of northern Australia (Figure 10c). According to Wheeler and Hendon (2004),
468 phases 5-7 (phases 2-3) are the active (suppressed) phases of the MJO over the northern Australian
469 region. Outside these dominant phases, there are widespread high pressure anomalies in the dry
470 surge composites exceeding +1.0 hPa over most of the domain associated with weak easterly

anomalies (Figure 10b). On the other hand, low pressure anomalies (-0.1 to -0.9 hPa) and relatively weak westerly anomalies are found over most of northern Australia in the wet surge composites (Figure 10d).

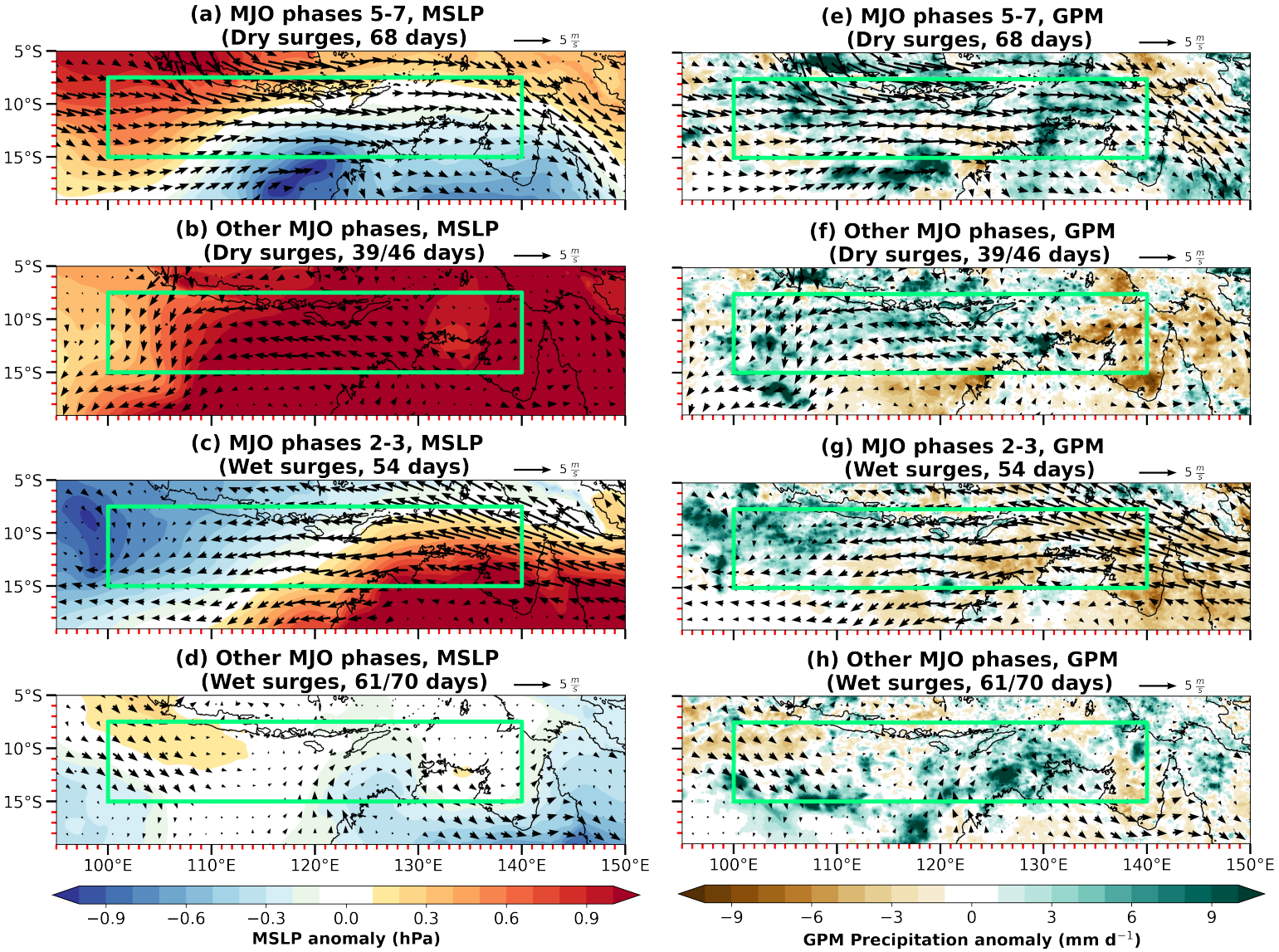


*Figure 10: Composite maps of daily mean (a-d) MSLP anomalies and (e-h) GPM precipitation anomalies with the seasonal cycle removed. Daily mean 925 hPa horizontal wind anomaly vectors. Dry and wet cold surges in both the dominant phases of the MJO (a, c, e, g), and all other phases including non-MJO days (b, d, f, h). The Australian monsoon domain is depicted by the green box. Cold surges that coincide with strong tropical cyclones over northern Australia within the non-dominant/non-MJO phases are removed.*

GPM rainfall patterns over the Australian monsoon domain are also largely influenced by the MJO patterns. Strongly enhanced precipitation anomalies (exceeding +10 mm $d^{-1}$ in some

476 areas) are most widespread during the active phases of the MJO (Figure 10e) while dry anomalies
477 are found over much of northern Australia in the suppressed phases (-1 to -7 mm $d^{-1}$; Figure 10g).
478 Outside the dominant phases, negative precipitation anomalies are found over much of northern
479 Australia in the dry surge composites (Figure 10f; peaking close to -10 mm $d^{-1}$), whereas patches
480 of strongly enhanced precipitation anomalies are found in the wet surge composites (Figure 10h).
481 The strongly enhanced precipitation anomalies here appear to be less connected to monsoon bursts
482 compared to the dry surge composites in phases 5-7 of the MJO since the westerly anomalies are
483 relatively weak.

484 From vertical profiles of zonal winds (Figure 11a), westerlies peak around 900 hPa in all
485 cases, but are strongest (close to 5 m $s^{-1}$) in the dry surge composites and weakest in the non-surge
486 composites. In the dry and moderate surge composites, the westerlies extend to approximately 450
487 hPa, which is close to the 'deep westerly regime' profile in Pope et al. (2009), who investigated
488 the regimes of the wet season in northern Australia. In their study, westerlies reach 350 hPa before
489 transitioning to easterlies. On the other hand, the wet surge and non-surge composites depict only
490 shallow westerlies, from the surface to approximately 800 hPa, and their zonal wind profiles are
491 similar. Meridional winds (Figure 11b) are generally weak (<1 m $s^{-1}$) in all composites throughout
492 most of the troposphere, although northerly winds (peaking close to -0.5 m $s^{-1}$) are found from

493 1000 to 900 hPa in the dry surge composites, which are likely a result of cross-equatorial flow
494 from cold surges.

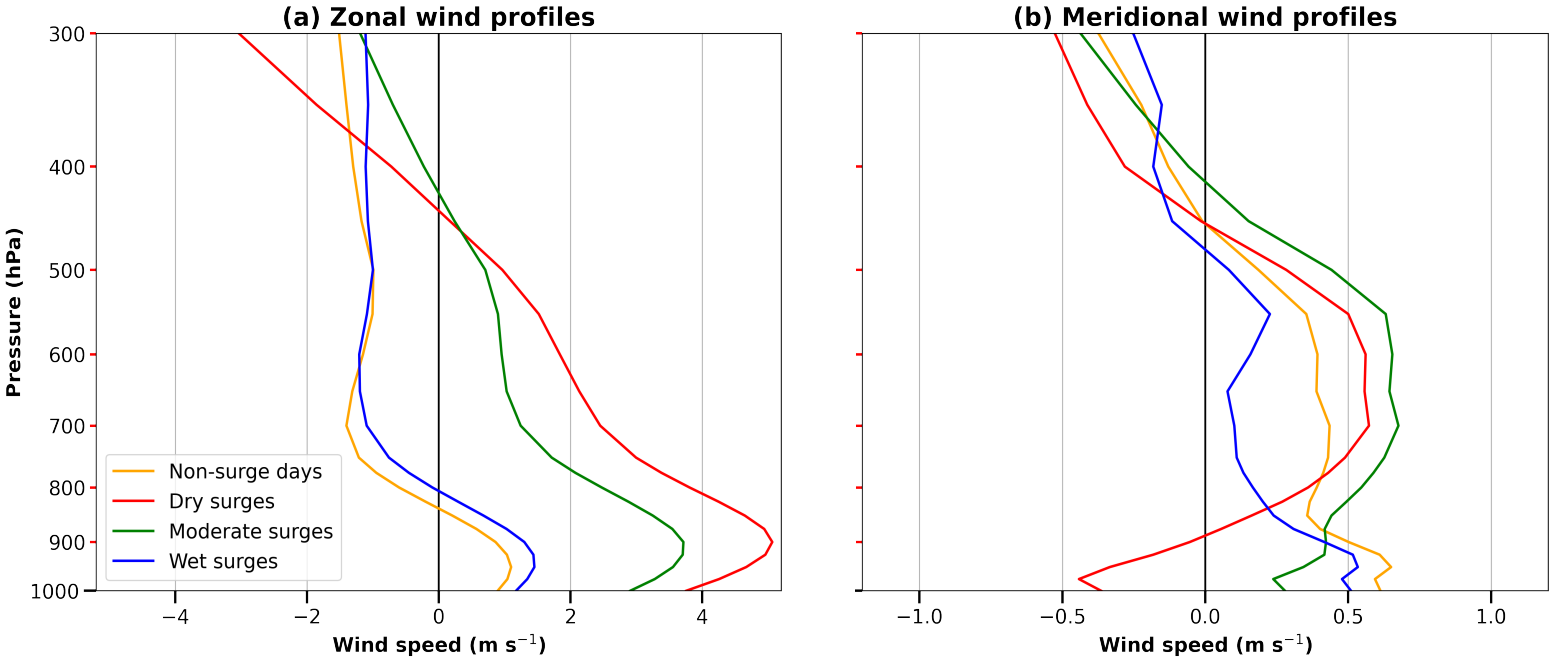


*Figure 11: Vertical profiles of (a) zonal and (b) meridional winds from 1000 to 300 hPa averaged over the Australian monsoon domain. Non-surge days (orange), and dry (red), moderate (green), and wet (blue) cold surge composites.*

495 From these results, the MJO appears to be the primary influence of the cross-equatorial
496 flow from cold surges, westerlies, and Australian summer monsoon bursts. This is also consistent
497 with the finding that most dry (wet) surges according to the precipitation domain coincide with
498 phases 5-7 (phases 2-3) of the MJO. The MJO influence also explains why the majority of cases
499 within the dry surge composites would be associated with westerlies and bursts in the Australian
500 summer monsoon and vice versa in the wet surge composites. Cross-equatorial surges can also be
501 thought of as the westerly part of the MJO. While the influences of cross-equatorial flow from cold
502 surges and the effects of the MJO cannot be separated, the westerlies over Australia are better
503 explained as part of MJO circulations rather than cold surges. The MJO influence over the
504 Australian summer monsoon is also consistent with findings from Berry and Reeder (2016) and
505 Narsey et al. (2017).

## 6 Conclusions

In this study, we analysed the synoptic structure and development of dry, moderate, and wet cold surges over the Maritime Continent region over 20 November-March seasons. The study included an investigation of both the seasonal and diurnal cycles. We also examined the relationship between the MJO and cold surges and bursts in the Australian summer monsoon.

The plume buoyancy, introduced by Adames et al. (2021), was used to better understand the convection associated with cold surges, and to delineate the three categories studied. In the 20-year climatology, there is an exponential increase in precipitation as $B_L$ increases towards zero, as found by Adames et al. (2021). Most wet surge days exceed the -0.02 m $s^{-2}$ threshold for $B_L$ and vice versa for most dry surge days. The diurnal cycle of $B_L$ is also consistent with that of GPM precipitation anomalies, and is suppressed over the precipitation domain. Strongly enhanced wet anomalies are found over much of the precipitation domain and equatorial South China Sea in the wet surges throughout the day, especially during the nocturnal hours. Our findings imply that the wet surges are characterised by a moister free troposphere that allows convection to penetrate through the lower troposphere.

In terms of synoptic environments, cold surges over the northern South China Sea are generally characterised by negative TCWV anomalies, and enhanced descent from negative 700 hPa ω anomalies. For the dry surge composites, enhanced descent or weaker ascent and dry air reach the precipitation domain, and enhanced ascent and moist air over Java. In the wet surge composites, the meridional TCWV anomaly gradient is located further to the north where the anomalies are positive over the precipitation domain. Here, the moist anomalies prior to surge onset are also consistent with our plume buoyancy results. The large areas of strongly enhanced ascent is also consistent with GPM precipitation anomaly patterns.

529 There is also a rapid acceleration of north-easterly wind anomalies towards the equator
530 associated with the cold surge, but negative $\theta_{e925}$ anomalies associated with the Siberian high
531 outflow are advected more slowly. Here, the propagation of the surge may be viewed as a transient
532 motion under the adjustment of the pressure-wind imbalance. In the vertical, descent with cold
533 and dry anomalies deepen and strengthen between day -1 and day +1, and are strongest and most
534 widespread in the dry surge composites. Warm and moist anomalies are most widespread near the
535 equator on day +1 in the wet surge composites, and the vertical gradient in $\theta_e$ anomalies means
536 that the lowest layers of the atmosphere are potentially stable. The corresponding precipitation
537 anomalies just to the north of the equator peak at approximately +45 mm $d^{-1}$.

538 Most of the dry surges occur during the suppressed phases of the MJO (phases 5-7) while
539 most of the wet surges occur during the active phases (phases 2-3). When the suppressed phases
540 of the MJO are over the precipitation domain in the dry surge composites, westerly anomalies
541 coincide with high-pressure anomalies over Java and low-pressure anomalies over northern
542 Australia. Here, the influence of cross-equatorial surges and the MJO on westerlies and the bursts
543 in the Australian summer monsoon is clearest, which is also evident from the areas of strongly
544 enhanced precipitation anomalies in these regions. The lack of cross-equatorial flow and westerlies
545 outside phases 5-7 coincide with widespread high-pressure anomalies extending to Java and
546 northern Australia. In the wet surge composites, weak low-pressure anomalies are observed over
547 much of the equatorial region during the active phases. The cyclonic circulation near Borneo in
548 the wet surge composites coincides with the large area of strongly enhanced precipitation
549 anomalies over the equatorial South China Sea, and a lack of cross-equatorial flow compared to
550 the dry surge composites. Over northern Australia, strong high-pressure anomalies are found with
551 low pressure anomalies over Java in MJO phases 2-3, which is opposite to the MSLP gradient in

552 phases 5-7 for the dry composites. Overall, the MJO appears to be the primary influence in
553 producing cross-equatorial flow, and the associated precipitation and westerlies in the Australian
554 summer monsoon.

555 Finally, deep westerlies are evident over the northern Australia domain in both the dry and
556 moderate surge composites, while shallow westerlies are found in the wet surge composites and
557 climatology. Northerly winds are also found between 1000 and 900 hPa in the dry surge
558 composites, which are likely a result of cross-equatorial flow associated with an active phase of
559 the MJO (phases 5-7 over northern Australia).

560 **Acknowledgments**

561 Tan was funded by the Monash International Tuition Scholarship (MITS) and the Maxwell King
562 PhD Scholarship. Birch and Peatman were funded by the Natural Environmental Research Council
563 (NERC) large grant, TerraMaris (NE/R016739/1). Birch was also funded by the Systematic
564 Analysis of Real Time Forecasts (FORSEA) project, funded by the Met Office Weather and
565 Climate Science for Service Partnership (WCSSP) Southeast Asia, as part of the Newton Fund.
566 We are grateful for the use of the National Computational Infrastructure (NCI) facilities to analyse
567 ERA5 data that was originally downloaded from the Copernicus Climate Change Service (C3S)
568 Climate Data Store, GPM-IMERG data from Goddard Earth Sciences Data and Information
569 Services Centre and the Wheeler-Hendon MJO index from the Australian Bureau of Meteorology.

570 **Open Research**

571 Data Availability Statement

572 All data used in this manuscript are publicly available. The ERA5 dataset is publicly available at
573 https://www.ecmwf.int/en/forecasts/datasets/reanalysis-datasets/era5, and the National
574 Computational Infrastructure (NCI) supercomputer (https://nci.org.au/) was remotely accessed to

575 analyse the ERA5 datasets from the rt52 workspace. The NASA GPM data may be obtained from
576 https://doi.org/10.5067/GPM/IMERGDF/DAY/06 for daily data and
577 https://doi.org/10.5067/GPM/IMERG/3B-HH/06 for half-hourly data. Daily MJO data are
578 available from the Australian Bureau of Meteorology at http://www.bom.gov.au/climate/mjo/.

579 **References**

580 Abdillah, M. R., Kanno, Y., Iwasaki, T., & Matsumoto, J. (2021). Cold Surge Pathways in East
581 Asia and Their Tropical Impacts. *Journal of Climate, 34*(1), 157-170.
582 https://journals.ametsoc.org/view/journals/clim/34/1/jcliD200552.xml

583

584 Adames, Á. F., Powell, S. W., Ahmed, F., Mayta, V. C., & Neelin, J.D. (2021). Tropical
585 Precipitation Evolution in a Buoyancy-Budget Framework, *Journal of the Atmospheric Sciences,*
586 *78*(2), 509-528. https://doi.org/10.1175/JAS-D-20-0074.1

587

588 Ahmed, F., & Neelin, J. D. (2018). Reverse Engineering the Tropical Precipitation–Buoyancy
589 Relationship. *Journal of the Atmospheric Sciences, 75*(5), 1587-1608.
590 https://journals.ametsoc.org/view/journals/atsc/75/5/jas-d-17-0333.1.xml

591

592 Argüeso, D., Romero, R., & Homar, V. (2020). Precipitation Features of the Maritime Continent
593 in Parameterized and Explicit Convection Models. *Journal of Climate, 33*(6), 2449-2466.
594 https://doi.org/10.1175/JCLI-D-19-0416.1

595

596 Berry, G. J., & Reeder, M. J. (2016). The Dynamics of Australian Monsoon Bursts. *Journal of the*
597 *Atmospheric Sciences, 73*(1), 55-69. https://doi.org/10.1175/JAS-D-15-0071.1

598

599 Chang, C.-P., Erickson, J. E., & Lau, K. M. (1979). Northeasterly Cold Surges and Near-Equatorial
600 Disturbances over the Winter MONEX Area during December 1974. Part I: Synoptic Aspects.
601 *Monthly Weather Review, 107*(7), 812-829. https://doi.org/10.1175/1520-
602 0493(1979)107<0812:NCSANE>2.0.CO;2
603
604 Chang, C.-P., Harr, P. A., & Chen, H.-J. (2005). Synoptic Disturbances over the Equatorial South
605 China Sea and Western Maritime Continent during Boreal Winter. *Monthly Weather Review,*
606 *133*(3), 489-503. https://doi.org/10.1175/MWR-2868.1
607
608 Chang, C.-P., Liu, C.-H., & Kuo, H.-C. (2003). Typhoon Vamei: An equatorial tropical cyclone
609 formation. *Geophysical Research Letters, 30*(3).
610 https://agupubs.onlinelibrary.wiley.com/doi/abs/10.1029/2002GL016365
611
612 Chang, C.-P., Lu, M.-M., & Wang, S. (2004). THE EAST ASIAN WINTER MONSOON. In *The*
613 *Global Monsoon System* (pp. 99-109).
614
615 Chang, C.-P., Millard, J. E., & Chen, G. T. J. (1983). Gravitational Character of Cold Surges during
616 Winter MONEX. *Monthly Weather Review, 111*(2), 293-307. https://doi.org/10.1175/1520-
617 0493(1983)111<0293:GCOCSD>2.0.CO;2
618
619 Davidson, N. E., McBride, J. L., & McAvaney, B. J. (1983). The Onset of the Australian Monsoon
620 During Winter MONEX: Synoptic Aspects. *Monthly Weather Review, 111*(3), 496-516.
621 https://doi.org/10.1175/1520-0493(1983)111<0496:TOOTAM>2.0.CO;2
622

de Rooy, W. C., & Siebesma, A. P. (2010). Analytical expressions for entrainment and detrainment in cumulus convection. *Quarterly Journal of the Royal Meteorological Society, 136*(650), 1216-1227. https://rmets.onlinelibrary.wiley.com/doi/abs/10.1002/qj.640

Ding, Y.H. (1994). *Monsoons over China*. Boston: Kluwer Academic Publishers, 91-173.

Fong, M. and Ng, L.K. (2012). *The weather and climate of Singapore*. Singapore: Meteorological Service Singapore, 70-97.

Gregory, D. (2001). Estimation of entrainment rate in simple models of convective clouds. *Quarterly Journal of the Royal Meteorological Society, 127*(571), 53-72. https://rmets.onlinelibrary.wiley.com/doi/abs/10.1002/qj.49712757104

Hersbach, H., Bell, B., Berrisford, P., Hirahara, S., Horányi, A., Muñoz-Sabater, J., et al. (2020). The ERA5 global reanalysis. *Quarterly Journal of the Royal Meteorological Society, 146*(730), 1999-2049. https://rmets.onlinelibrary.wiley.com/doi/abs/10.1002/qj.3803

Huffman, G. J., Bolvin, D. T., Braithwaite, D., Hsu, K., Joyce, R., Kidd, C., Nelkin, E. J., Sorooshian, S., Tan, J., & Xie, P. (2019). NASA Global Precipitation Measurement (GPM) Integrated Multi-satellitE Retrievals for GPM (IMERG), Algorithm Theoretical Basis Document (ATBD) Version 06. *National Aeronautics and Space Administration*.

645 Johnson, R. H., & Chang, C.-P. (2007). WINTER MONEX: A Quarter-Century and Beyond.
646 *Bulletin of the American Meteorological Society, 88*(3), 385-388. www.jstor.org/stable/26217263
647
648 Johnson, R. H., & Houze, R. A., Jr. (1987). Precipitating cloud systems of the Asian monsoon.
649 *Monsoon Meteorology*. https://ci.nii.ac.jp/naid/10014597164/en/
650
651 Lau, K.-M., & Li, M.-T. (1984). The Monsoon of East Asia and its Global Associations—A
652 Survey. *Bulletin of the American Meteorological Society, 65*(2), 114-125.
653 https://doi.org/10.1175/1520-0477(1984)065<0114:TMOEAA>2.0.CO;2
654
655 Lim, H., & Chang, C.-P. (1981). A Theory for Midlatitude Forcing of Tropical Motions during
656 Winter Monsoons. *Journal of the Atmospheric Sciences, 38*(11), 2377-2392.
657 https://doi.org/10.1175/1520-0469(1981)038<2377:ATFMFO>2.0.CO;2
658
659 Lim, S. Y., Marzin, C., Xavier, P., Chang, C.-P., & Timbal, B. (2017). Impacts of Boreal Winter
660 Monsoon Cold Surges and the Interaction with MJO on Southeast Asia Rainfall. *Journal of*
661 *Climate, 30*(11), 4267-4281. https://doi.org/10.1175/JCLI-D-16-0546.1
662
663 Love, G. (1985). Cross-Equatorial Influence of Winter Hemisphere Subtropical Cold Surges.
664 *Monthly Weather Review, 113*(9), 1487-1498. https://doi.org/10.1175/1520-
665 0493(1985)113<1487:CEIOWH>2.0.CO;2
666
667 Meteorological Service Singapore [MSS]. (2022). *Weather Systems*. Retrieved 8 August, 2022,
668 from http://www.weather.gov.sg/learn_weather_systems/

669

670 Meteorological Service Singapore [MSS]. (2022a). *2021 Annual Climate Assessment Singapore.*
671 Retrieved 8 August 2022, from http://www.weather.gov.sg/climate-annual-climate-reports/

672

673 Narsey, S., Reeder, M. J., Ackerley, D., & Jakob, C. (2017). A Midlatitude Influence on Australian
674 Monsoon Bursts. *Journal of Climate, 30*(14), 5377-5393. https://doi.org/10.1175/JCLI-D-16-
675 0686.1

676

677 Narsey, S., Reeder, M. J., Jakob, C., & Ackerley, D. (2018). An Evaluation of Northern Australian
678 Wet Season Rainfall Bursts in CMIP5 Models. *Journal of Climate, 31*(19), 7789-7802.
679 https://doi.org/10.1175/JCLI-D-17-0637.1

680

681 National Aeronautics and Space Administration [NASA]. (2021). *Global Precipitation*
682 *Measurement*. Retrieved 4 February, 2021, from https://gpm.nasa.gov/data-
683 access/downloads/gpm

684

685 Neale, R., & Slingo, J. (2003). The Maritime Continent and Its Role in the Global Climate: A
686 GCM Study. *Journal of Climate, 16*(5), 834-848. https://doi.org/10.1175/1520-
687 0442(2003)016<0834:TMCAIR>2.0.CO;2

688

689 Pope, M., Jakob, C., & Reeder, M. J. (2009). Regimes of the North Australian Wet Season.
690 *Journal of Climate, 22*(24), 6699-6715.
691 https://journals.ametsoc.org/view/journals/clim/22/24/2009jcli3057.1.xml

692

693 Pullen, J., Gordon, A. L., Flatau, M., Doyle, J. D., Villanoy, C., & Cabrera, O. (2015). Multiscale
694 influences on extreme winter rainfall in the Philippines. *Journal of Geophysical Research:*
695 *Atmospheres, 120*(8), 3292-3309.
696 https://agupubs.onlinelibrary.wiley.com/doi/abs/10.1002/2014JD022645

697

698 Ramage, C. S. (1968). ROLE OF A TROPICAL "MARITIME CONTINENT" IN THE
699 ATMOSPHERIC CIRCULATION1. *Monthly Weather Review, 96*(6), 365-370.
700 https://doi.org/10.1175/1520-0493(1968)096<0365:ROATMC>2.0.CO;2
701 Ramage, C.S. (1971). *Monsoon Meteorology*. London: Academic Press, 229-242.

702

703 Raymond, D., Fuchs, Ž., Gjorgjievska, S., & Sessions, S. (2015). Balanced dynamics and
704 convection in the tropical troposphere. *Journal of Advances in Modeling Earth Systems, 7*(3),
705 1093-1116. https://agupubs.onlinelibrary.wiley.com/doi/abs/10.1002/2015MS000467

706

707 Suppiah, R., & Wu, X. (1998). Surges, cross-equatorial flows and their links with the Australian
708 summer monsoon circulation and rainfall. *Australian Meteorological Magazine, 47*(2), 113-130.

709

710 Tangang, F. T., Juneng, L., Salimun, E., Vinayachandran, P. N., Seng, Y. K., Reason, C. J. C., et
711 al. (2008). On the roles of the northeast cold surge, the Borneo vortex, the Madden-Julian
712 Oscillation, and the Indian Ocean Dipole during the extreme 2006/2007 flood in southern
713 Peninsular Malaysia. *Geophysical Research Letters, 35*(14).
714 https://agupubs.onlinelibrary.wiley.com/doi/abs/10.1029/2008GL033429

715

716 Wheeler, M. C., & Hendon, H. H. (2004). An All-Season Real-Time Multivariate MJO Index:
717 Development of an Index for Monitoring and Prediction. *Monthly Weather Review, 132*(8),
718 1917-1932. https://journals.ametsoc.org/doi/abs/10.1175/1520-
719 0493%282004%29132%3C1917%3AAARMMI%3E2.0.CO%3B2
720
721 Wu, P., Hara, M., Fudeyasu, H., Yamanaka, M. D., Matsumoto, J., Syamsudin, F., et al. (2007).
722 The Impact of Trans-equatorial Monsoon Flow on the Formation of Repeated Torrential Rains
723 over Java Island. *SOLA, 3*, 93-96. https://doi.org/10.2151/sola.2007-024
724
725 Xavier, P., Lim, S. Y., Ammar Bin Abdullah, M. F., Bala, M., Chenoli, S. N., Handayani, A. S.,
726 et al. (2020). Seasonal Dependence of Cold Surges and their Interaction with the Madden–Julian
727 Oscillation over Southeast Asia. *Journal of Climate, 33*(6), 2467-2482.
728 https://doi.org/10.1175/JCLI-D-19-0048.1
729
730 Yang, J.H., Qian, J.H., & Timbal, B. (2019). A moisture flux perspective on cold surges and wet
731 spells affecting Singapore. *MSS Research Letters*. Issue 3, 3-9. Retrieved 4 February, 2021, from
732 http://ccrs.weather.gov.sg/wp-content/uploads/2019/07/MRL_Issue_3_Jul2019_FINAL.pdf
733 \Yihui, D. (1990). Build-up, air mass transformation and propagation of Siberian high and its
734 relations to cold surge in East Asia. *Meteorology and Atmospheric Physics, 44*(1), 281-292.
735 https://doi.org/10.1007/BF01026822
736
737 Yihui, D. (1994). *Monsoons over China*. Boston: Kluwer Academic Publishers, 91-173.

# FIGURE CAPTION GUIDE

**Figure 1**. The figure caption should begin with an overall descriptive statement of the figure followed by additional text. They should be immediately after each figure. Figure parts are indicated with lower-case letters (**a, b, c…**). For initial submission, please place both the figures and captions in the text near where they are cited rather than at the end of the file (not both). At revision, captions can be placed in-text or at the end of the file, and figures should be uploaded separately. Each figure should be one complete, cohesive file (please do not upload sub-figures or figure parts in separate files.